Chemical Science



EDGE ARTICLE

View Article Online
View Journal | View Issue



Cite this: Chem. Sci., 2024, 15, 15769

dll publication charges for this article have been paid for by the Royal Society of Chemistry

Received 9th June 2024 Accepted 25th August 2024

DOI: 10.1039/d4sc03780d

rsc.li/chemical-science

Rationally engineering a binary SnS_{0.5}Se_{0.5}/carbon nest-coated Si nanosphere for a high-performance lithium-ion battery anode†

Hui Zhang,^a Kehao Tao,^{bc} Xiangbing Zeng,^d Chengbing Chen,^d Yajun Zhu,^{ae} Tianli Han,^a Jinjin Li ^b *^b and Jinyun Liu ^b *^a

Although the silicon (Si) anode has a high theoretical capacity, large volume-expansion would lead to rapid capacity decay. Here, a core-nest structured Si@SnS $_{0.5}$ Se $_{0.5}$ /carbon (Si@SnS $_{0.5}$ Se $_{0.5}$ /C) is developed using silicon as the core and SnS $_{0.5}$ Se $_{0.5}$ /carbon as a binary nest. Both the core-nest structure and carbon matrix enable a stable hybrid structure during charge and discharge. The binary nest Si@SnS $_{0.5}$ Se $_{0.5}$ /C nanospheres as a lithium-ion battery anode display good capacity, recoverable rate-performance, and enhanced electron and ion transfer properties. A capacity of 1318 mA h g $^{-1}$ and a high coulombic efficiency of 98.9% after 50 cycles at 0.1 A g $^{-1}$ are achievable, and the capacity remains 887 mA h g $^{-1}$ after 150 cycles at 0.5 A g $^{-1}$. A high capacity at 50 °C is also retained, showing a high initial specific capacity. It is found that the reaction resistance of Si@SnS $_{0.5}$ Se $_{0.5}$ /C is significantly lower than that of the pure components, and the stress–strain relationship of the Li–Si system is demonstrated by density functional theory (DFT) calculations. The engineering of the binary-nest structure should be able to provide some new ideas for developing many other high-performance energy-storage hybrids.

Introduction

Silicon (Si) as a lithium-ion (Li-ion) battery anode has the advantage of high specific capacity, which is quite attractive. ¹⁻³ However, the large volumetric change upon lithiation-delithiation leads to powdering and continuous solid electrolyte interphase (SEI) formation. ⁴ The repeated volumetric change during cycling would cause poor electrical contact and safety issues. ⁵ The low conductivity and high Li-ion transmission resistance, ⁶⁻⁹ as well as the fracture and pulverization of the Si alloy particles, ¹⁰ result in severe capacity fading. Recently, tremendous efforts have been made to address these critical issues. It is considered that engineering nanostructures and designing Si-based hybrids could improve the electrochemical performance. ^{11,12}

Many Si-based nanohybrids have been reported, such as egg yolk/double-shell Si composites, ^{13,14} ant nest-shaped porous Si, ¹⁵ hollow Si microspheres and carbon nanotube (a)Si. ^{16,17} Since small Si has a small volumetric change compared to large ones,

and it is beneficial for enhancing Li⁺ ion diffusion and electron transport, investigations using small-sized Si for constructing composites have received much attention.¹⁸ Of course, the high activity of small particles should be of concern as they would generate by-products with the electrolyte during charge and discharge. Tin (Sn) is considered to be promising for Li-ion battery anodes because of its low cost (about 20 USD kg⁻¹), large capacity (993.4 mA h g⁻¹) and environmental friendliness.19,20 Although the introduction of Sn for the Si anode would improve the conductivity and performance,21,22 the volumetric change of Sn may also lead to pulverization and the formation of a nonstable solid electrolyte interphase (SEI). It is considered that combining Sn-based compounds with some conductive materials (such as carbon) can buffer the volumetric expansion, and prevent aggregation.23-25 However, the density of Sn is higher than that of Si and graphite. Therefore, the energy density of the integrated Li-ion battery would be decreased. Since then, in order to get ideally balanced performances, the optimal amount and appropriate Sn-based component used in the anode should be well considered and studied.26

^eKey Laboratory of Functional Molecular Solids, Ministry of Education, College of Chemistry and Materials Science, Anhui Normal University, Wuhu, Anhui 241002, PR China. E-mail: jyliu@ahnu.edu.cn

^bNational Key Laboratory of Science and Technology on Micro/Nano Fabrication, Department of Micro/Nano-electronics, Shanghai Jiao Tong University, Shanghai 200240, PR China. E-mail: lijinjin@sjtu.edu.cn

Department of Micro/Nano Electronics, School of Electronic Information and Electrical Engineering, Shanghai Jiao Tong University, Shanghai, 200240, PR China

^dAnhui Deeiot Energy Technology Co., Ltd, Wuhu, Anhui 241002, PR China

^eInstitute of Energy, Hefei Comprehensive National Science Center, Hefei, Anhui 230031. PR China

[†] Electronic supplementary information (ESI) available. See DOI: https://doi.org/10.1039/d4sc03780d

Several sulfides, such as SnS, are considered to be able to provide good transportation channels and high specific capacity for batteries, but they suffer from volumetric changes leading to severe structural collapse. Therefore, constructing composites by working with selenides would be an efficient strategy, which can induce rich phase boundaries and increase electrochemical reactive sites. In addition, applying both Se and S elements would improve the reaction kinetics.²⁷ Although Se and S locate in the same main group and have similar chemical properties, Se shows a smaller band gap and larger ionic radius, which could improve the intrinsic electronic conductivity, widen the lattice spacing of the sulfide and generate new anion defect sites for promoting ionic storage. It also helps to optimize the diffusion pathway of Li⁺ ions and avoid excessive surface reactions.²⁸ Considering that, optimal engineering of Si anodes working with some surface modification components would achieve ideal electrochemical performances.

Here, we develop a Si-based hybrid containing Si nanoparticles as the core encapsulated by $SnS_{0.5}Se_{0.5}$ in the carbon layer (called $Si@SnS_{0.5}Se_{0.5}/C$). The hybrid would have the following features: (i) tin selenium sulfide could be able to provide high conductivity and abundant reactive sites; (ii) the core-nest structure is beneficial for the transport of Li^+ , and reduces internal resistance, enabling good cycling stability under different current densities; (iii) the binary $SnS_{0.5}Se_{0.5}/C$ layer prevents the direct contact between Si and the electrolyte, improving the structural stability. The results show that the $Si@SnS_{0.5}Se_{0.5}/C$ anode displays stable capacity and good rate-performance. It is found that the reaction resistance of $Si@SnS_{0.5}Se_{0.5}/C$ is low, indicating a good conductivity. The stress–strain relationship of the Li–Si system has also been investigated by first-principles modeling.

Results and discussion

A facile solvothermal method was used to synthesize a Si@MOF precursor (Fig. S1a-d†) coated on Si nanospheres (Fig. S1e and f[†]), which was sulfurized then selenized in a tube furnace, as shown in Fig. 1a. The morphology of Si@SnS_{0.5}Se_{0.5}/C was observed by scanning electron microscopy (SEM, Fig. 1b) and transmission electron microscopy (TEM, Fig. 1c-e, and S2†), exhibiting a spherical core-nest morphology. The coating layer has a thickness of 5-10 nm wrapping on the Si nanospheres as the core. The surface layer as a nest is porous and uniformly coated on Si, which would facilitate the contact with the electrolyte and buffer the volumetric change of the Si core during cycling. X-ray powder diffraction (XRD) patterns confirm the crystal phases of Si@SnS_{0.5}Se_{0.5}/C, SnS_{0.5}Se_{0.5}/C, and Si (Fig. S3†). Seen from the high-resolution TEM (HRTEM) image (Fig. 1f), lattice spacings of 0.305 and 0.288 nm correspond to the (011) and (111) planes of SnS_{0.5}Se_{0.5}, respectively. The selected area electron diffraction (SAED) pattern (Fig. 1g) indicates a polycrystalline structure. The core-nest structure and rich phase boundaries would provide high-speed channels for Li⁺ transfer.²⁹ The elemental mappings show that the elements distribute uniformly in Si@SnS_{0.5}Se_{0.5}/C (Fig. 1h and S4†). Fig. S4d† shows the elemental contents of Si, Sn, S, Se and C,

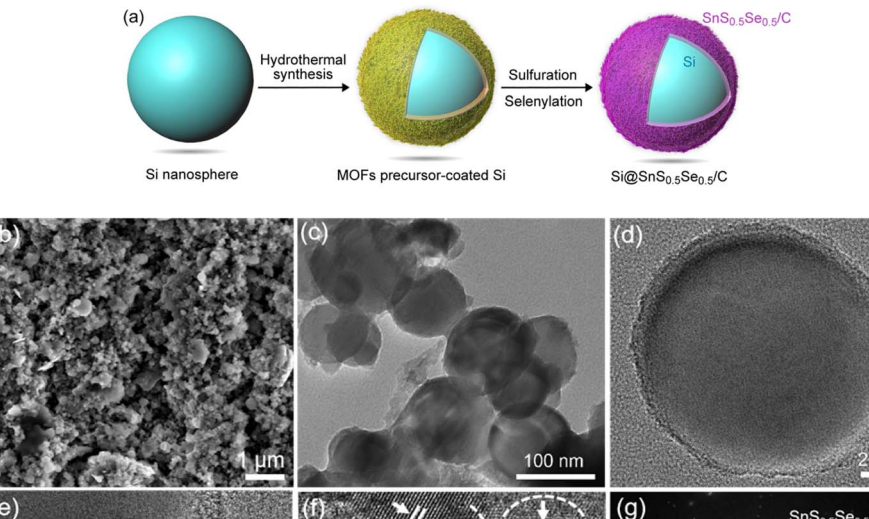
which are 14.25%, 11.7%, 1.33%, 4.76% and 67.96%, respectively.

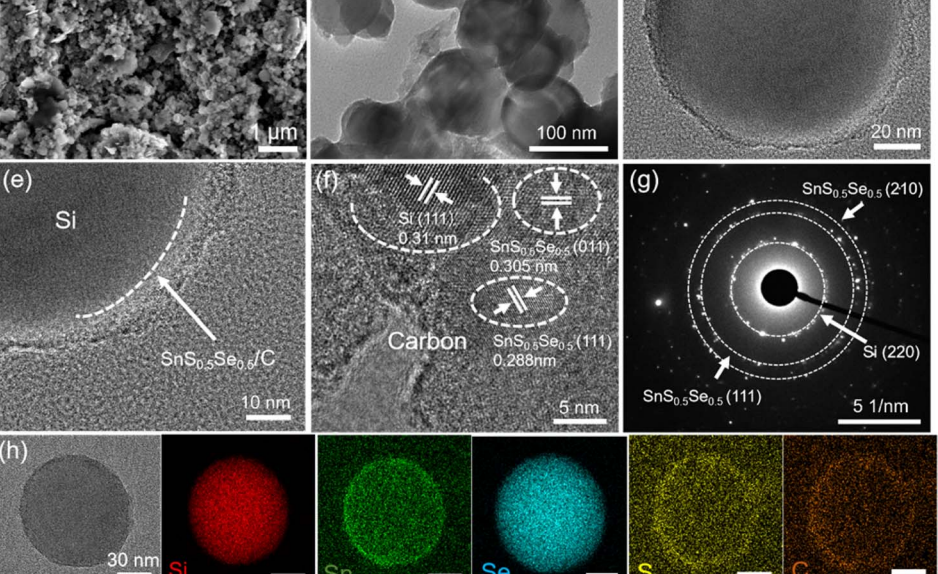
In the Raman spectrum of Si@SnS_{0.5}Se_{0.5}/C (Fig. S5†), the bands at 508.4 and 935.0 cm⁻¹ correspond to the Si.^{30,31} The bands at 1350.5 and 1589.5 cm⁻¹ are assigned to carbon, and they correspond to the D and G bands, respectively. The relative crystallinity is determined by the intensity ratio of the G and D bands (I_D/I_G) .³² It is noted that I_D/I_G (0.59) of Si@SnS_{0.5}Se_{0.5}/C is close to that of $SnS_{0.5}Se_{0.5}/C$ ($I_D/I_G = 0.57$), which indicates that the coating of Si would not influence the carbon structure. In Fig. S6,† the Brunauer-Emmett-Teller (BET) specific surface area of Si@SnS_{0.5}Se_{0.5}/C is 52.93 m² g⁻¹, which is larger compared to pure Si (39.26 m² g⁻¹), while it is lower than that of $SnS_{0.5}Se_{0.5}/C$ (92.24 m² g⁻¹), which was prepared for comparison as shown in Fig. S7.† Although high specific surface area and porosity reduce the diffusion paths for ions, the relatively large specific surface area would cause side reactions for the Si anodes with the electrolyte, forming a non-stable SEI film. This indicated that the presented composite has a moderate specific surface area and is favorable for improving the cycling stability of Li-ion batteries.

X-ray photoelectron spectroscopy (XPS) and electron diffraction spectroscopy (EDS) spectra were used to investigate the surface electronic state and composition. In Fig. 2a, the XPS survey spectrum shows that Si@SnS_{0.5}Se_{0.5}/C contains Si, Sn, S, Se and C, which is in agreement with the EDS result (Fig. 1h). The Si 2p spectrum presents four peaks at 98.9, 99.1, 100.3 and 102.8 eV, which are ascribed to Si $2p_{3/2}$, Si $2p_{1/2}$, Si-C, and Si-O, respectively (Fig. 2b). In the Sn 2p spectrum (Fig. 2c), two peaks at 495.8 and 487.4 eV are assigned to Sn 3d_{3/2} and Sn 3d_{5/2}, respectively, suggesting a valence state of +2 Sn.³³ It is noted that the Sn 3d peaks shift toward lower binding energy for Si@SnS_{0.5}Se_{0.5}/C, which is ascribed to the fact that the Sn-Se bond is longer than Sn-Sn, and the Sn atoms are more electronggative than the Se atoms. This is also confirmed in the S 2p spectrum.27 The Se 3d spectrum (Fig. 2d) shows peaks at 53.6 and 55.7 eV that are indexed to Se 3d_{5/2} and Se 3d_{3/2}, respectively. The peaks in the S 2p spectrum at 163.1 and 164.2 eV in Fig. 2e are indexed to $2p_{3/2}$ and $2p_{1/2}$ of S^{2-} , respectively. The carbon spectrum (Fig. 2f) shows peaks at 284.7, 286.5 and 289.0 eV, which are assigned to C-C/C=C, C=O and O-C=O, respectively.

Cyclic voltammetry (CV) curves of the Si $@SnS_{0.5}Se_{0.5}/C$ anode are presented in Fig. 3a. The small reduction peak at 1.16 V is ascribed to Li⁺ intercalation into the interlayers of $SnS_{0.5}Se_{0.5}/C$, ³⁴ and generates Li_x $SnS_{0.5}Se_{0.5}$ in the first cathodic scan. ³⁵ The peak at 1.16 V disappears while a strong reduction peak located at approximately 1.3 V appears and remains in subsequent cycles, which is originated from the irreversible decomposition of $SnS_{0.5}Se_{0.5}$ during the first lithiation process. ³⁶ A broad reduction peak is observed from 0.5 to 0 V, which is attributed to the reversible transformation of Li_x- $SnS_{0.5}Se_{0.5}$. Additionally, a cathodic peak at 0.14 V appears, related to the lithiation of Si to form Li_xSi (0 $\leq x \leq$ 4.4). ³⁷ Moreover, an irreversible SEI layer is formed on the surface of Si $@SnS_{0.5}Se_{0.5}/C$, which undergoes an electrochemical alloying reaction between Sn, Si and Li. ³⁸ During the first de-lithiation

Edge Article





 $\textbf{Fig. 1} \quad \textbf{(a) Illustration of the preparation of Si@SnS}_{0.5} \textbf{Se}_{0.5} / \textbf{C} \ \ \text{hybrid nanospheres. (b) SEM image of Si@SnS}_{0.5} \textbf{Se}_{0.5} / \textbf{C}. \ \ \textbf{(c-e) TEM and (f) HRTEM } \\ \textbf{Se}_{0.5} \textbf{Se}_{0.5} / \textbf{C}. \ \ \textbf{(c-e) TEM and (f) HRTEM } \\ \textbf{Se}_{0.5} \textbf{Se}_{0.5} / \textbf{C}. \ \ \textbf{(c-e) TEM and (f) HRTEM } \\ \textbf{Se}_{0.5} \textbf{Se}_{0.5} / \textbf{C}. \ \ \textbf{(c-e) TEM and (f) HRTEM } \\ \textbf{Se}_{0.5} \textbf{Se}_{0.5} / \textbf{C}. \ \ \textbf{(c-e) TEM and (f) HRTEM } \\ \textbf{Se}_{0.5} \textbf{Se}_{0.5} / \textbf{C}. \ \ \textbf{(c-e) TEM and (f) HRTEM } \\ \textbf{Se}_{0.5} \textbf{Se}_{0.5} / \textbf{C}. \ \ \textbf{(c-e) TEM and (f) HRTEM } \\ \textbf{Se}_{0.5} \textbf{Se}_{0.5} / \textbf{C}. \ \ \textbf{(c-e) TEM and (f) HRTEM } \\ \textbf{Se}_{0.5} \textbf{Se}_{0.5} / \textbf{C}. \ \ \textbf{(c-e) TEM and (f) HRTEM } \\ \textbf{Se}_{0.5} \textbf{Se}_{0.5} / \textbf{C}. \ \ \textbf{(c-e) TEM and (f) HRTEM } \\ \textbf{Se}_{0.5} \textbf{Se}_{0.5} / \textbf{C}. \ \ \textbf{(c-e) TEM and (f) HRTEM } \\ \textbf{Se}_{0.5} \textbf{Se}_{0.5} / \textbf{C}. \ \ \textbf{(c-e) TEM and (f) HRTEM } \\ \textbf{Se}_{0.5} \textbf{Se}_{0.5} / \textbf{C}. \ \ \textbf{(c-e) TEM and (f) HRTEM } \\ \textbf{Se}_{0.5} \textbf{Se}_{0.5} / \textbf{C}. \ \ \textbf{(c-e) TEM and (f) HRTEM } \\ \textbf{Se}_{0.5} \textbf{Se}_{0.5} / \textbf{C}. \ \ \textbf{(c-e) TEM and (f) HRTEM } \\ \textbf{Se}_{0.5} \textbf{Se}_{0.5} / \textbf{C}. \ \ \textbf{(c-e) TEM and (f) HRTEM } \\ \textbf{Se}_{0.5} \textbf{Se}_{0.5} / \textbf{C}. \ \ \textbf{(c-e) TEM and (f) HRTEM } \\ \textbf{Se}_{0.5} \textbf{Se}_{0.5} / \textbf{C}. \ \ \textbf{(c-e) TEM and (f) HRTEM } \\ \textbf{Se}_{0.5} \textbf{Se}_{0.5} / \textbf{C}. \ \ \textbf{(c-e) TEM and (f) HRTEM } \\ \textbf{Se}_{0.5} \textbf{Se}_{0.5} / \textbf{C}. \ \ \textbf{(c-e) TEM and (f) HRTEM } \\ \textbf{Se}_{0.5} \textbf{Se}_{0.5} / \textbf{C}. \ \ \textbf{(c-e) TEM and (f) HRTEM } \\ \textbf{Se}_{0.5} \textbf{Se}_{0.5} \textbf{Se}_{0.5} / \textbf{C}. \ \ \textbf{(c-e) TEM and (f) HRTEM } \\ \textbf{Se}_{0.5} \textbf{Se$ photographs, (g) corresponding SAED pattern, and (h) TEM photograph and mappings of Si@SnS_{0.5}Se_{0.5}/C.

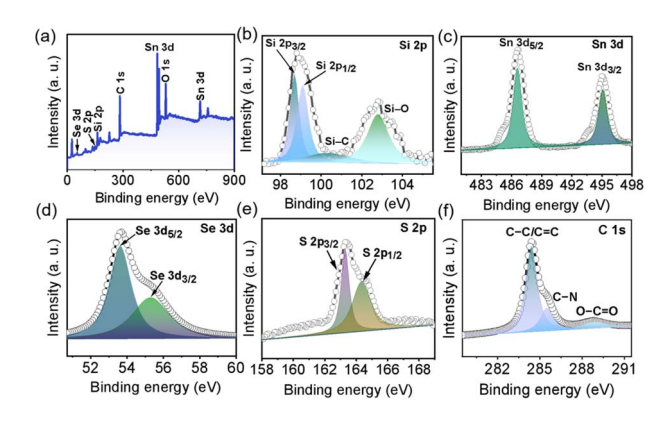


Fig. 2 (a) XPS survey spectrum of $Si@SnS_{0.5}Se_{0.5}/C$. XPS spectra of (b) Si 2p, (c) Sn 3d, (d) Se 3d, (e) S 2p, and (f) C 1s.

process, oxidation peaks from 0 to 0.8 V appear due to the dealloying effect of LixSn. Two oxidation peaks at 0.35 and 0.57 V are observed, which are attributed to the delithiation of Li_xSi to form Si. As the peak of SnS_{0.5}Se_{0.5} becomes weak gradually and finally disappears, the crystalline phases of Li_xSnS and Li_xSnSe become obvious, indicating that the peak near 1.8 V is attributed to the reversible conversion of SnSe and SnS. After

the first cycle, the CV profiles follow a similar shape, indicating that improved performance is achievable through the inhibition of irreversible redox by implementing suitable modifications.²⁸ For comparison, CV curves of the SnS_{0.5}Se_{0.5}/C (Fig. S8†) and pure Si anodes (Fig. S9†) were also investigated, which displays poor reversibility compared to the Si@SnS_{0.5}Se_{0.5}/C. The reactions of the Si@SnS_{0.5}Se_{0.5}/C anode are presented below:

$$SnS_{0.5}Se_{0.5} + xLi^{+} + xe^{-} \rightleftharpoons Li_{x}SnS_{0.5}Se_{0.5}$$
 (1)

$$\text{Li}_x \text{SnS}_{0.5} \text{Se}_{0.5} + x \text{Li}^+ + x \text{e}^- \rightleftharpoons \text{Li}_x \text{SnSe} + \text{Li}_x \text{SnS}$$
 (2)

$$\text{Li}_x \text{SnSe} + \text{Li}_x \text{SnS} + x \text{Li}^+ + x \text{e}^- \rightleftharpoons \text{Li}_x \text{Se} + \text{Li}_x \text{S} + x \text{Sn}$$
 (3)

$$Sn + xLi^{+} + xe^{-} \rightleftharpoons Li_{x}Sn \tag{4}$$

$$Si + xLi^+ + xe^- \rightleftharpoons Li_xSi$$
 (5)

$$C + xLi^{+} + xe^{-} \rightleftharpoons Li_{x}C$$
 (6)

Fig. 3b shows the charge-discharge curves of the Si@SnS_{0.5}Se_{0.5}/C anode at 0.1 A g^{-1} . In the first two cycles, the

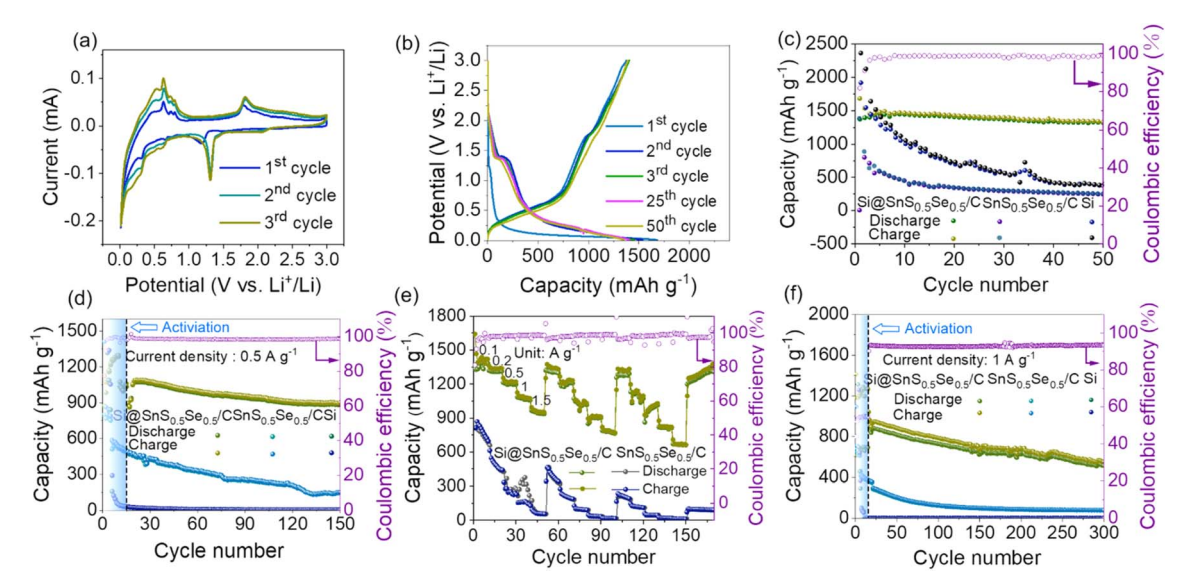


Fig. 3 (a) CV profiles of the Si@SnS $_{0.5}$ Se $_{0.5}$ /C anode at a scanning rate of 0.1 mV s $^{-1}$. (b) Charge–discharge profiles of Si@SnS $_{0.5}$ Se $_{0.5}$ /C upon cycling at 0.1 A g $^{-1}$. Capacities of Si@SnS $_{0.5}$ Se $_{0.5}$ /C, SnS $_{0.5}$ Se $_{0.5}$ /C and Si at (c) 0.1 and (d) 0.5 A g $^{-1}$. Coulombic efficiencies were from Si@SnS $_{0.5}$ Se $_{0.5}$ /C. The anodes were pre-cycled for 10 cycles at 0.1 A g $^{-1}$ for activation. (e) Rate-performance of the Si@SnS $_{0.5}$ Se $_{0.5}$ /C and SnS $_{0.5}$ Se $_{0.5}$ /C anodes. (f) Long-term cyclability of Si@SnS $_{0.5}$ Se $_{0.5}$ /C, SnS $_{0.5}$ Se $_{0.5}$ /C and Si at 1.0 A g $^{-1}$. The anodes were pre-cycled for 15 cycles at 0.1 A g $^{-1}$ for activation.

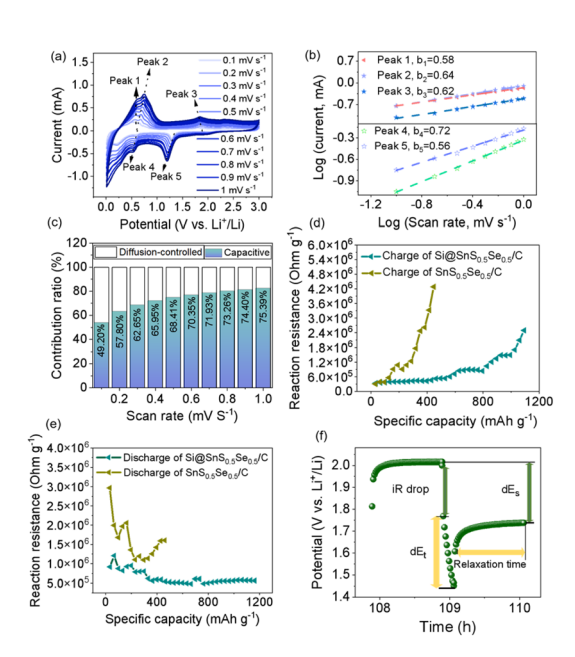


Fig. 4 (a) CV curves at 0.1 to 1.0 mV s⁻¹. (b) Log(i) vs. log(v) of the oxidization and reduction peaks, and (c) ratio of the contributions. In situ reaction impedances of Si@SnS_{0.5}Se_{0.5}/C and SnS_{0.5}Se_{0.5}/C during (d) discharge and (e) charge. (f) Illustration of ∂E_s , ∂E_t , and the iR drop.

Si \otimes SnS_{0.5}Se_{0.5}/C has obvious discharging plateaus at 0.2 and 1.3 V, and obvious charging ones at 0.5 and 1.8 V, which correspond to the CV curves. The first-cycle discharge capacity of Si \otimes SnS_{0.5}Se_{0.5}/C is 1680 mA h g⁻¹ and the charge capacity is 1374 mA h g⁻¹, exhibiting an initial coulombic efficiency (CE) of 81.8%. After the first few cycles, the CE is high, indicating that the SEI film is stable.³⁹ In Fig. 3c, it shows 1318 mA h g⁻¹ with

a CE as high as 98.9% after 50 cycles. Cycling under a high current density of 0.5 A g⁻¹, the Si@SnS_{0.5}Se_{0.5}/C anode maintains 887 mA h g⁻¹ with a CE as high as 98.6% after 150 cycles (Fig. 3d). In contrast, the SnS_{0.5}Se_{0.5}/C and Si anodes show poor stability. It is considered that the synergistic effect of SnS_{0.5}Se_{0.5} with carbon and Si nanospheres contributes to the enhancement of the electrochemical performance. This is ascribed to the core-nest structure of the composite, which buffers the volumetric change during the insertion and extraction of Li+ ions.40 Moreover, the surface of the core-nest structure is porous, which accommodates the volumetric expansion of Si, thus reducing structural collapse. Fig. S10† shows that the CE is 99.6% after 100 cycles at 0.2 A g⁻¹, which is much higher than that of the bare Si nanospheres and SnS_{0.5}Se_{0.5}/C. The SEM images after cycling are shown in Fig. S11.† The hybrid maintains a spherical shape after cycling. The mapping images (Fig. S12†) verify that the composition has not changed after cycling, which is attributed to the protection layer of SnS_{0.5}Se_{0.5} in the carbon matrix. Fig. S13 and S14† show the SEM and TEM images of the post-cycled SnS_{0.5}Se_{0.5}/C and pure Si after cycling, respectively. Both of them transform obviously compared to the initial morphology, indicating a non-stable structure. The rate performances of the different anodes were studied under different current densities (Fig. 3e). High capacities and high CE for Si@SnS_{0.5}Se_{0.5}/C are achieved, which are much larger than the SnS_{0.5}Se_{0.5}/C. The capacity retention rate of $Si@SnS_{0.5}Se_{0.5}/C$ is also better than that of $SnS_{0.5}Se_{0.5}/C$ (Fig. 3f). Fig. S15† presents galvanostatic discharge-charge curves of the Si@SnS_{0.5}Se_{0.5}/C anode, showing overlapping profiles and small polarization. The battery with Si@SnS_{0.5}Se_{0.5}/C as the anode material shows a high initial CE at 50 °C. A capacity of 557 mA h g⁻¹ is maintained at 50 °C (Fig. S16†), which is

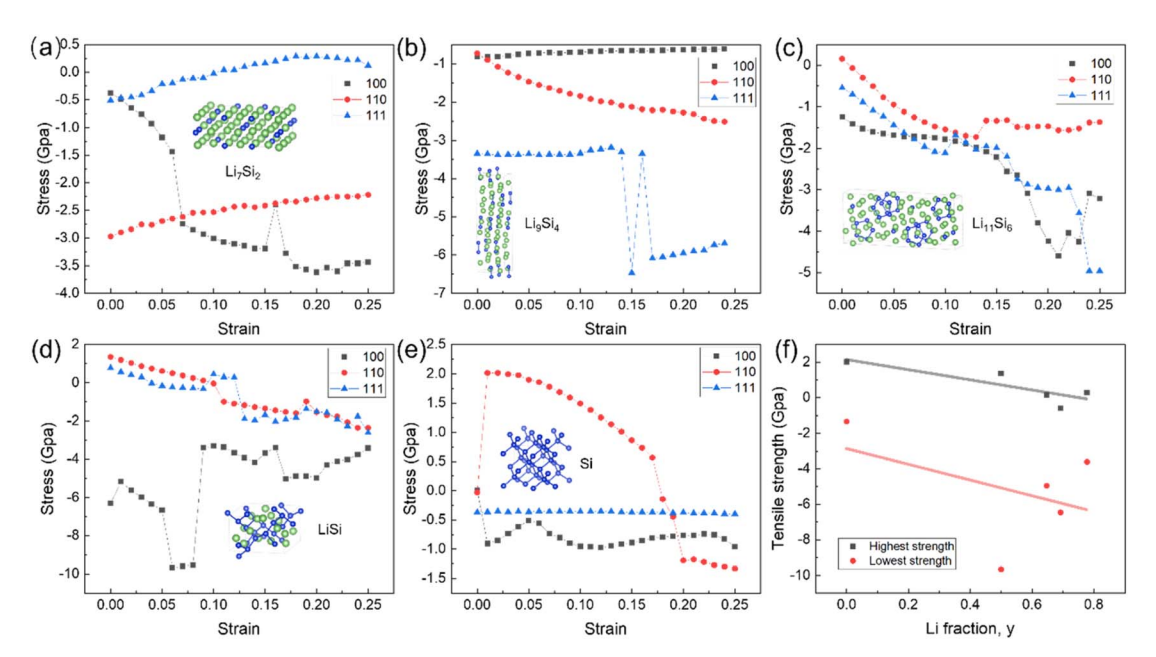


Fig. 5 The relationships of stress and strain in the Li–Si system with different Li and Si ratios: (a) Li_7Si_2 , (b) Li_9Si_4 , (c) $Li_{11}Si_6$, (d) LiSi, and (e) Si. The crystal structure was inserted in each figure. The green and blue spheres represent Li and Si atoms, respectively. (f) Relationships between maximum and minimum principal stress and the Li fraction.

ascribed to the binary nest structure of the $SnS_{0.5}Se_{0.5}$ nanoparticles embedded in the carbon matrix improving the conductivity and enhancing the interfacial stability of the developed hybrid system. However, although the initial capacity is high, the decay is obvious. This is perhaps ascribed to the non-stable electrolyte and interface properties of the electrode under a high temperature.

CV curves of the Si@SnS_{0.5}Se_{0.5}/C anode were measured at 0.1–1.0 mV s⁻¹ to study the electrochemical kinetics behaviors. In Fig. 4a, the CV curves display small polarization and high reversibility. The ratio of the capacitive contribution was calculated by relating the peak current (i) to the scan rate (v) i = av^b . Fig. 4b displays that the b values of Si@SnS_{0.5}Se_{0.5}/C at peaks 1-5 are 0.58, 0.64, 0.62, 0.72 and 0.56, respectively, indicating that the Li-ion storage kinetics are mainly dominated by capacitive behavior. On the basis of equations $i = k_1 v + k_2 v_{1/2}$ and $i/v_{1/2} = k_1v_{1/2} + k_2$, where k_1 and k_2 are constants and k_1v stands for the capacitive effect, the capacitive contribution was calculated by using $k_1 v/(k_1 v + k_2 v_{0.5})$. The capacitive contribution increases from 49.2% to 75.4% depending on the elevation of the scanning rate (Fig. 4c). It is considered that a large pseudocapacitance contribution benefits rate-performance and stability. Fig. 4d and e show the in situ internal resistance during charge and discharge. The internal resistance of the hybrid is much lower than that of the pure Si and SnS_{0.5}Se_{0.5}/C. Fig. S17† displays the galvanostatic intermittent titration technique (GITT) results of the Si@SnS_{0.5}/C anode. Fig. S18a-c† show the internal resistance and GITT diagram at high temperature, which show that the internal resistance is small even at a high-temperature environment. Electrochemical impedance spectroscopy (EIS) analysis was conducted further, and the charge transfer resistance (R_{ct}) was analyzed

(Fig. S19a†). The transfer resistance ($R_{\rm ct}$) of Si@SnS_{0.5}Se_{0.5}/C is \approx 319 Ω , which is low compared to SnS_{0.5}Se_{0.5}/C (1190 Ω) and Si (1178 Ω). After cycling 100 times, the $R_{\rm ct}$ of Si@SnS_{0.5}Se_{0.5}/C remains small (Fig. S19b†). The charge transfer resistance of Si@SnS_{0.5}Se_{0.5}/C is reduced due to the nest structure, which enhances the electronic conductivity. Fig. 4f shows individual work steps in the GITT measuring process.

In addition, the stress-strain relationship was investigated by density of functional theory (DFT) calculations on the Li-Si system, as shown in Fig. 5. The tensile stress is between 0 and 2 GPa. Fig. 5a-e shows the stress and strain of the Li-Si system under different Li fractions (from high to low), where the curves of different colors show the stress and strain in different directions. It can be seen that the stress changes in the system with higher Li content, and when the Si content increases, the stress changes with a positive correlation. The curve shows an irregular negative correlation trend, indicating that the increase of the Li content may improve the stress-strain performance of the Li-Si system. In Fig. 5f, the maximum tensile stress of Si along the (110) direction is 2 GPa, which is higher than any other selected Li-Si system in the corresponding direction. The stress on different planes increases depending on the increase of the strain, and tends to be stable when the strain is about 0.2. The principal stress of the Li-Si structure is shown in Fig. 5f. The Li fraction y is defined as the ratio of Li atom x in Li_xSi to all atoms, i.e., y = x/(1 + x) alloys. The tensile strength decreases with the increase of the Li concentration, which indicates that the proportion of Li atoms has a great influence on the mechanical properties of the Li-Si alloy. Considering that, an optimal surface coating is significant for especially the initial period of lithiation, which indicates that the binary-nest structure coating on Si would enable mild Li⁺ diffusion, which keeps

a stable stress equilibrium during the initial alloying between Si and Li. Finally, a stable Li–Si system was obtained with the difference of the Li–Si content and the increase of the Li content.

Conclusions

In summary, we developed a Si@SnS $_{0.5}$ Se $_{0.5}$ /C hybrid composed of a Si core encapsulated in a binary-nest SnS_{0.5}Se_{0.5}/C matrix. Such engineering of the Si@SnS_{0.5}Se_{0.5}/C reduces the structure collapse during charge and discharge, and enables a stable SEI layer, thus achieving good cycling performances with high and stable capacity of 1318 mA h g⁻¹ and coulombic efficiency of 98.9% after 50 cycles at 0.1 A g^{-1} , and 887 mA h g^{-1} after 150 cycles at 0.5 A g⁻¹. The Si@SnS_{0.5}Se_{0.5}/C hybrid anode also exhibits high and stable capacities during rate-performance measurements, which are much better compared to SnS_{0.5}Se_{0.5}/C and pure Si anodes. The DFT calculations on stress and strain indicate that the binary-nest coating would optimize the Li-ion diffusion during alloying between silicon and lithium. It is expected that these findings, including the structural core-binary nest design and the composition, will provide a new way to develop energy-storage materials with high electrochemical performances.

Data availability

The data supporting this article have been included as part of the ESI.†

Author contributions

J. Y. L conceived the project. J. Y. L and H. Z wrote the manuscript. H. Z performed the characterizations and performance tests. K. H. T and J. J. L performed the modeling and data analysis. X. B. Z, C. B. C, Y. J. Z and T. L. H participated in the experiments and analysis.

Conflicts of interest

There are no conflicts to declare.

Acknowledgements

This work was supported by the Major Science and Technology Research Project of Anhui Province (2023z020003), Cooperation Funding for Long Cycle Life and High-Capacity Battery Materials (901-852309), Anhui Provincial Quality Engineering Projects (2022xqhz020 and 2023qygzz007), Shanghai Science and Technology Project (21JC1403400 and 23JC1402300), and Natural Science Research Project for Universities in Anhui Province (2022AH050176).

Notes and references

- 1 G. G. Eshetu, H. Zhang, X. Judez, H. Adenusi, M. Armand, S. Passerini and E. Figgemeier, *Nat. Commun.*, 2021, **12**, 5459.
- 2 J. Guo, D. Dong, J. Wang, D. Liu, X. Yu, Y. Zheng, Z. Wen, W. Lei, Y. Deng, J. Wang, G. Hong and H. Shao, *Adv. Funct. Mater.*, 2021, 31, 2102546.
- 3 M. Ge, C. Cao, G. M. Biesold, C. D. Sewell, S. M. Hao, J. Huang, W. Zhang, Y. Lai and Z. Lin, *Adv. Mater.*, 2021, 33, 2004577.
- 4 K. Feng, M. Li, W. W. Liu, A. G. Kashkooli, X. C. Xiao, M. Cai and Z. W. Chen, *Small*, 2018, **14**, 1702737.
- 5 L. Y. Beaulieu, T. D. Hatchard, A. Bonakdarpour, M. D. Fleischauer and J. R. Dahn, *J. Electrochem. Soc.*, 2003, 150, A1457–A1464.
- 6 M. N. Obrovac and V. L. Chevrier, *Chem. Rev.*, 2014, **114**, 11444–11502.
- 7 Z. Du, R. A. Dunlap and M. N. Obrovac, J. Electrochem. Soc., 2014, 161, A1698–A1705.
- 8 J. H. Ryu, J. W. Kim, Y. E. Sung and S. M. Oh, *Electrochem. Solid State Lett.*, 2004, 7, A306.
- 9 H. Wu and Y. Cui, Nano Today, 2012, 7, 414-429.
- 10 K. Rhodes, N. Dudney, E. Lara-Curzio and C. Daniel, J. Electrochem. Soc., 2010, 157, A1354.
- 11 L. Su, Y. Jing and Z. Zhou, Nanoscale, 2011, 3, 103967.
- 12 Z. Wu, J. Luo, J. Peng, H. Liu, B. Chang and X. Wang, *Green Energy Environ.*, 2021, 6, 4517.
- 13 X. Xiao, J. S. Wang, P. Liu, A. K. Sachdev, M. W. Verbrugge, D. Haddad and M. P. Balogh, *J. Power Sources*, 2012, **04**, 28.
- 14 W. Lu, X. Guo, Y. Luo, Q. Li, R. Zhu and H. Pang, *Chem. Eng. J.*, 2019, 355, 208–237.
- 15 W. An, B. Gao, S. Mei, B. Xiang, J. Fu, L. Wang, Q. Zhang, P. K. Chu and K. Huo, *Nat. Commun.*, 2019, **10**, 1447.
- 16 Z. Chao, L. Zhao, Z. Ze, J. Cai, Z. Yang and Y. Ji, Chem. Phys. Lett., 2021, 138566.
- 17 Y. Fan, Q. Zhang, C. Lu, Q. Xiao, X. Wang and B. K. Tay, *Nanoscale*, 2013, 5, 41503.
- 18 F. Wu, Y. Dong, Y. F. Su, C. X. Wei, T. R. Chen, W. G. Yan, S. Y. Ma, L. Ma, B. Wang, L. Chen, Q. Huang, D. Y. Cao, Y. Lu, M. Wang, L. Wang, G. Q. Tan, J. H. Wang and N. Li, Small, 2023, 19, 2301301.
- 19 Q. Pan, Y. Huang, H. Wang, G. Yang, L. Wang, J. Chen, Y. Zan and Q. Li, *Electrochim. Acta*, 2016, **197**, 50–57.
- 20 F. Zhang, C. Xia, J. Zhu, B. Ahmed, H. Liang, D. B. Velusamy, U. Schwingenschlogl and H. N. Alshareef, *Adv. Energy Mater.*, 2016, 6, 1601188.
- 21 C. Zhu, Y. Zhang, Z. Wu, Z. Ma, X. Guo, F. Guo, J. Zhang and Y. Li, *J. Mater. Sci. Technol.*, 2021, 8718.
- 22 B. Ma, J. Luo, X. Deng, Z. Wu, Z. Luo, X. Wang and Y. Wang, *ACS Appl. Nano Mater.*, 2018, **1**(12), 6989.
- 23 H. Ying, S. Zhang, Z. Meng, Z. Sun and W. Q. Han, J. Mater. Chem., 2017, 5, A8334–A8342.
- 24 Y. Yu, L. Gu, C. Zhu, P. A. Van Aken and J. Maier, *J. Am. Chem. Soc.*, 2009, **131**, 15984–15985.

Edge Article

- 26 H. Yoo, J. H. Moon, H. Seong, Y. Jin, G. Kim, T. Jung, J. B. Lee, S. kwon, M. Yang and J. Choi, *J. Energy Storage*, 2024, 96, 112599.
- 27 X. Hu, M. Qiu, Y. J. Liu, J. Yuan, J. X. Chen, H. B. Zhang and Z. H. Wen, *Adv. Energy Mater.*, 2022, **12**, 2202318.
- 28 Y. Wang, C. X. Xu, X. T. Tian, S. Y. Wang and Y. Zhao, *Chin. J. Struct. Chem.*, 2023, 42, 100167.
- 29 L. Lia, J. Zhou and C. Zhang, Comp. Commun., 2019, 15, 162167.
- 30 N. Lin, T. Xu, T. Li, Y. Han and Y. Qian, ACS Appl. Mater. Interfaces, 2017, 9, 39318–39325.
- 31 S. K. Kim, H. Kim, H. Chang, B. G. Cho, J. Huang, H. Yoo, H. Kim and H. D. Jang, *Sci. Rep.*, 2016, **6**, 33688.
- 32 G. Q. Zhao, C. F. Li, X. Wu, J. G. Yu, X. Y. Jiang, W. J. Hu and F. P. Jiao, *Appl. Surf. Sci.*, 2018, **434**, 251–259.

- 33 D. Chao, C. Zhu, P. Yang, X. Xia, J. Liu, J. Wang and X. Fan, *Nat. Commun.*, 2016, 7, 12122.
- 34 Q. M. Tang, Y. H. Cui and J. W. Wu, *Nano Energy*, 2017, **41**, 377-386.
- 35 G. D. Park, J. H. Kim and Y. C. Kang, *Mater. Charact.*, 2016, **120**, 349–356.
- 36 Q. M. Tang, H. Su, Y. H. Cui, A. P. Bakera, Y. C. Liu, J. Lua, X. N. Song and H. Y. Zhang, *J. Power Sources*, 2018, 379, 182–190.
- 37 D. Q. Zhang, J. F. Ren, C. X. Li, B. Luo, L. Wang and Y. Y. Li, *Chin. J. Struct. Chem.*, 2022, 41, 2205055–2205062.
- 38 D. Han, S. Xu, J. Li, B. Liu, G. Song and Z. Guo, *Mater. Lett.*, 2017, **199**, 93–96.
- 39 Y. Xing, T. Shen, T. Guo, X. Wang, X. Xia, C. Gu and J. Tu, *J. Power Sources*, 2018, **384**, 207–214.
- 40 S. W. Chai, X. Xiao, Y. B. Li and C. H. An, *Chin. J. Struct. Chem.*, 2022, **41**, 2208018–2208024.